2018

The Impact of Sensor Response and Airspeed on the Representation of the Convective Boundary Layer and Airmass Boundaries by Small Unmanned Aircraft Systems

Adam L. Houston

Jason M. Keeler

The Impact of Sensor Response and Airspeed on the Representation of the Convective Boundary Layer and Airmass Boundaries by Small Unmanned Aircraft Systems

ADAM L. HOUSTON AND JASON M. KEELER[a]

Department of Earth and Atmospheric Sciences, University of Nebraska–Lincoln, Lincoln, Nebraska

(Manuscript received 9 February 2018, in final form 25 June 2018)

ABSTRACT

The objective of the research presented is to assess the impact of sensor response and aircraft airspeed on the accuracy of in situ observations collected by small unmanned aircraft systems profiling the convective boundary layer or transecting airmass boundaries. Estimates are made using simulated aircraft flown within large-eddy simulations. Both instantaneous errors (differences between observed temperature, which include the effects of sensor response and airspeed, and actual temperature) and errors in representation (differences between serial observations and representative snapshots of the atmospheric state) are considered. Synthetic data are retrieved assuming a well-aspirated first-order sensor mounted on rotary-wing aircraft operated as profilers in a simulated CBL and fixed-wing aircraft operated through transects across a simulated airmass boundary. Instantaneous errors are found to scale directly with sensor response time and airspeed for both CBL and airmass boundary experiments. Maximum errors tend to be larger for airmass boundary transects compared to the CBL profiles. Instantaneous errors for rotary-wing aircraft profiles in the CBL simulated for this work are attributable to the background lapse rate and not to turbulent temperature perturbations. For airmass boundary flights, representation accuracy is found to degrade with decreasing airspeed. This signal is most pronounced for flights that encounter the density current wake. When representation errors also include instantaneous errors resulting from sensor response, instantaneous errors are found to be dominant for flights that remain below the turbulent wake. However, for flights that encounter the wake, sensor response times generally need to exceed ~5 s before instantaneous errors become larger than errors in representation.

1. Introduction

In recent years, there has been a rapid expansion in the use of small unmanned aircraft systems (sUAS) in atmospheric field studies as a result of their ability to obtain targeted, in situ thermodynamic and kinematic observations. These systems are particularly beneficial when flight conditions have the potential to pose substantial safety risks to an onboard pilot. Such flights could be hazardous for larger or manned aircraft because of characteristics of the flight path (e.g., low altitude) or characteristics of the environment to be sampled. For these reasons, most recent sUAS applications have focused on atmospheric phenomena in the atmospheric boundary layer (Houston et al. 2012; Kiefer et al. 2012; van den Kroonenberg et al. 2012; Reineman et al. 2013; Knuth and Cassano 2014; Riganti and Houston 2017).

As with any in situ observations, sUAS observations are prone to error when sampling phenomena characterized by strong spatial gradients. These errors should theoretically scale directly with the speed at which an aircraft passes across a gradient and with the sensor response time τ, typically defined as the e-folding response. While errors stemming from "slow" sensors could be minimized in postprocessing (e.g., McCarthy 1973; Burns et al. 1999), the aim of this work is to offer practical guidance on the configuration and operation of airborne systems that are required to maximize the accuracy of observations of boundary layer phenomena without substantial postprocessing.

Serial observations collected by in situ platforms are typically used to approximate the state of a phenomenon at a given time (a snapshot). However, this approximation degrades for phenomena that evolve over a time scale less than the observation period, a degradation that can occur even when sensors have near-zero response

[a] Current affiliation: Department of Earth and Atmospheric Sciences, Central Michigan University, Mount Pleasant, Michigan.

Corresponding author: Dr. Adam L. Houston, ahouston2@unl.edu

DOI: 10.1175/JTECH-D-18-0019.1

times. For an airborne platform, the accuracy of representation of a particular snapshot should scale directly with airspeed. In contrast, as noted above, the instantaneous accuracy should scale inversely with airspeed. Another aim of this work is to characterize the representation accuracy as a function of aircraft airspeed.

Experiments for this work are conducted using simulated aircraft "flown" within large-eddy simulations (LES). This approach enables evaluation of synthetic observations (data representative of what could have been sampled had an actual instrument platform been deployed in an environment consistent with that simulated). A similar approach has been applied to evaluate the structure-function parameter for temperature using synthetic data sampled using sUAS flown in a helical ascent flight plan (Wainwright et al. 2015). In a broader sense, evaluations of synthetic observations from LES have also been applied to platforms/instrumentation, including boundary layer radar (Scipion et al. 2009), scintillometers (Maronga et al. 2013), lidar, and sodar (Lundquist et al. 2015). Experiments consider combinations of modeled sensor response as well as aircraft airspeed. Focus is directed toward two phenomena that are often the focus of targeted data collection by sUAS: the convective boundary layer (CBL) and airmass boundaries. Since the CBL is often observed using profiling by rotary-wing [also known as vertical takeoff and landing (VTOL)] aircraft (e.g., Hemingway et al. 2017), synthetic observations of the CBL are modeled using a simulated rotary-wing aircraft. Similarly, since airmass boundaries are often observed using transects by fixed-wing aircraft (e.g., Elston et al. 2011; Frew et al. 2012; Houston et al. 2012; Riganti and Houston 2017), synthetic observations of airmass boundaries are modeled using a simulated fixed-wing aircraft. For a review of atmospheric sampling using fixed-wing sUAS, including typical instrumentation, see Elston et al. (2015).

This article proceeds with a description of the experiment design, including the characteristics of both the large-eddy simulations and the procedure used for synthetic data retrieval by simulated rotary-wing and fixed-wing aircraft. In section 3, results are presented from experiments using rotary-wing aircraft in a CBL simulation and fixed-wing aircraft in an airmass boundary simulation. A discussion of the results is presented in section 4 and a summary follows in section 5.

2. Experiment design

a. Large-eddy simulations

Synthetic sUAS datasets were obtained from flights through two separate LES using the First-Generation Pennsylvania State University–National Center for Atmospheric Research Cloud Model, release 18.3 (CM1; Bryan and Fritch 2002). Both simulations use isotropic grids with a 50-m gridpoint spacing within the atmospheric boundary layer. Inclusion of radiative forcing, surface fluxes, a semislip lower boundary condition, and random thermal perturbations with magnitudes ≤ 0.1 K at all grid points in the lowest 1000 m enable the development of boundary layer convection and is similar to the approach adopted by Nowotarski et al. (2014). Insolation is consistent with mid-April in midlatitudes and is updated every 3 min within each simulation. Surface heat and moisture fluxes assume an irrigated cropland and pastureland surface type. The surface model is based on Monin–Obukhov (Monin and Obukhov 1954) with a Carlson–Boland (Carlson and Boland 1978) viscous sublayer and standard similarity functions from lookup tables; it is the same surface model used by the Weather Research and Forecasting Model (Skamarock et al. 2008) for "sf_surface_physics = 1." The reader is referred to Dudhia (1996) and Dudhia et al. (2004) for a full explanation of this surface model.

The CBL simulation is run on a $480 \times 480 \times 61$ point doubly periodic domain with a flat lower boundary and vertical level spacing that increases above a height of 2000 m from 50 to 200 m by 4000 m, and remains at 200 m through the domain top at 5000 m. The simulation is initialized at 1200 UTC (all times will be reported in UTC; local time is UTC minus 5 h) with an idealized sounding characterized by a surface $\theta = 294$ K, $d\theta/dz = 0.007\,\mathrm{K\,m^{-1}}$ through a height of 1200 m, an inversion between 1200 and 1250 m for which $d\theta/dz = 0.08\,\mathrm{K\,m^{-1}}$, well-mixed conditions between 1250 and 3200 m, and $d\theta/dz = 0.0033\,\mathrm{K\,m^{-1}}$ between 3200 m and the domain top at 5000 m. Initial vertical shear gradually decreases through 2000 UTC, the start time for analyses included herein, consistent with the deepening of a well-mixed CBL. At 2000 UTC the magnitude of the domain-averaged 0–1000-m vertical shear is $0.0024\,\mathrm{s^{-1}}$, which, paired with destabilization via strong surface heat fluxes, favored CBL convection organized as open-celled convection (Fig. 1a).

The airmass boundary simulation utilizes a pseudo-2D (west–east) domain covering $4864 \times 8 \times 100$ grid points. Periodic (open) boundary conditions are used in the south–north (west–east) direction. The model is initialized at 1800 UTC (as in the CBL simulation, local time is UTC minus 5 h) with a sounding that is well mixed through a height of 900 m. Inflow of laminar conditions at the eastern edge of the domain was prevented by setting $u = 2.5\,\mathrm{m\,s^{-1}}$ throughout the depth of the domain in the initial conditions. The density current and associated boundary are initialized using a dam

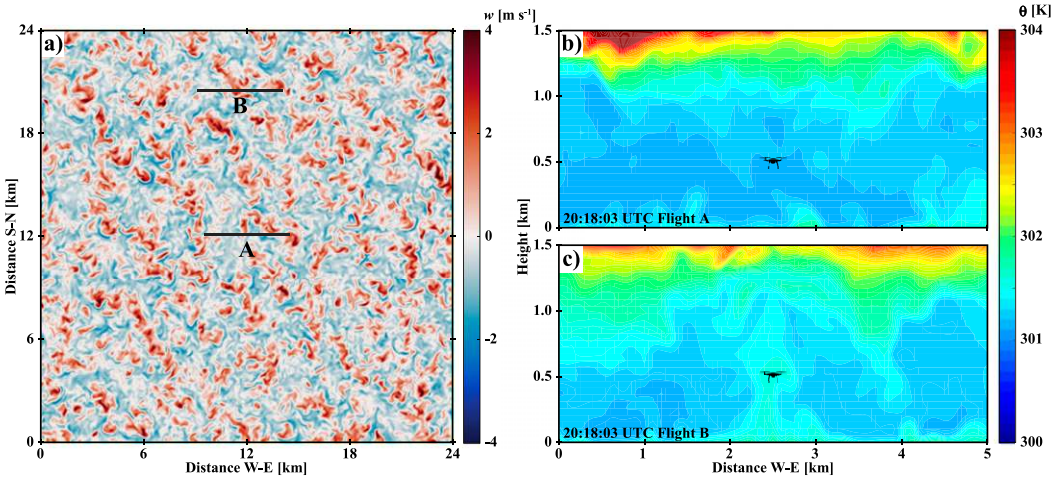

FIG. 1. (a) Plan view of vertical air velocity w in the CBL simulation at 2018:03 UTC (1518:03 LT) and $z = 750$ m. Vertical cross sections of potential temperature (shaded every 0.1 K) along with rotary-wing aircraft positions for (b) all flights at the domain center (flight A) and (c) in a thermal located 400 m west and 8500 m north of the domain center (flight B). The cross section locations are indicated by the W–E black lines in (a). Flights are located at the center of the lines.

break (e.g., Droegemeier and Wilhelmson 1987; Chen 1995; Liu and Moncrieff 1996; Lee and Wilhelmson 1997; Houston 2016) characterized by an initial 2000-m-deep cold dam with a maximum temperature perturbation of −15 K positioned along the western 25 km of the domain. Well-developed boundary layer thermals and density current structure are present during the analysis period (Fig. 2), which begins at 1930 UTC, 5400 s into the simulation.

b. Synthetic temperature retrieval

Both aircraft models have been designed to execute simple and physically reasonable trajectories through the atmospheric phenomena used for this work. The rotary-wing aircraft model constrains the aircraft to maintain a constant ground-relative ascent rate and fixed lateral position. Thus, the wind does not alter the position or ascent rate. Modern rotary-wing aircraft are capable of maintaining a fixed lateral position even in "moderate" and gusty winds. While the critical wind strength necessary to reliably maintain a fixed lateral position depends on aircraft size, this assumption is valid for the vast majority of typical CBL operations using sUAS. The parameter space for the CBL experiments with rotary-wing flights includes ascent rates ranging from 0.5 to 20 m s^{-1} (a total of 30 ascent rates are considered: 0.5, 1.0, 1.5, . . . , 10, 11, 12, . . . , 20 m s^{-1}). Flights are executed over an observation period centered at time t = 2018:03 UTC (Figs. 1b,c). Two sets of flights are conducted: "location A" has an x–y position at the center of the domain and "location B" has an x–y position 400 m west and 8500 m north of domain center (Fig. 1a). Location B corresponds to a position at which all flights pass through a strong boundary layer thermal. Flights begin at the lowest scalar grid point (z = 25 m) and terminate at z = 1000 m (only the ascending portion of each profile is used in the analysis).

The fixed-wing aircraft model constrains the aircraft to maintain a constant airspeed and fixed altitude; the ambient lateral wind can modify the aircraft ground speed but vertical motion does not force the aircraft to a different altitude or result in changes to airspeed. Actual fixed-wing aircraft will invariably experience small changes in altitude in the presence of vertical motion that characterizes both the CBL and airmass boundaries (e.g., Riganti and Houston 2017). However, associated temperature changes are expected to be small enough to justify exclusion in the methodology adopted for this work. The experiment parameter space includes airspeeds ranging from 4 to 100 m s^{-1} (a total of 32 airspeeds were considered: 4, 5, 6, . . . , 25, 30, . . . , 50, 60, 70, . . . , 100 m s^{-1}) and altitudes of 175, 475, and 725 m (Fig. 2). Flights begin in the warm sector either 500, 2000, 4000, or 6000 m ahead of the boundary (a distance referred to as δx_b). Each flight is configured to terminate approximately 5000 m into the cold air. However, because the actual wind field encountered by a simulated aircraft depends on the aircraft initial altitude and because boundary-relative displacement for a given wind field tends to exhibit more variability at slower prescribed airspeeds, the actual boundary-relative location of flight termination is not the same for every flight (Fig. 3).

Gridded simulated temperature is interpolated to aircraft position using trilinear interpolation. Interpolation

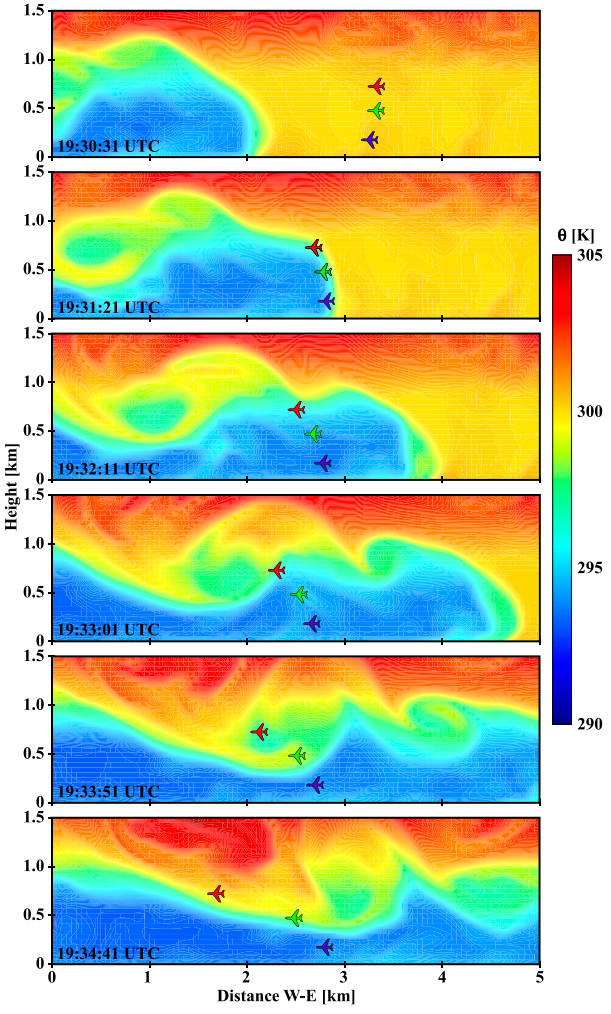

FIG. 2. Vertical cross sections of potential temperature (shaded every 0.1 K) for the airmass boundary simulation along with fixed-wing aircraft positions for flights with an airspeed of 20 m s^{-1}, δx_b of 2000 m, and z of 175 m (purple symbol), 475 m (green symbol), and 725 m (red symbol). Panel times are indicated (local time is UTC minus 5 h). The subdomain shown in this figure is between 115 950 and 120 950 m from the western edge of the model domain.

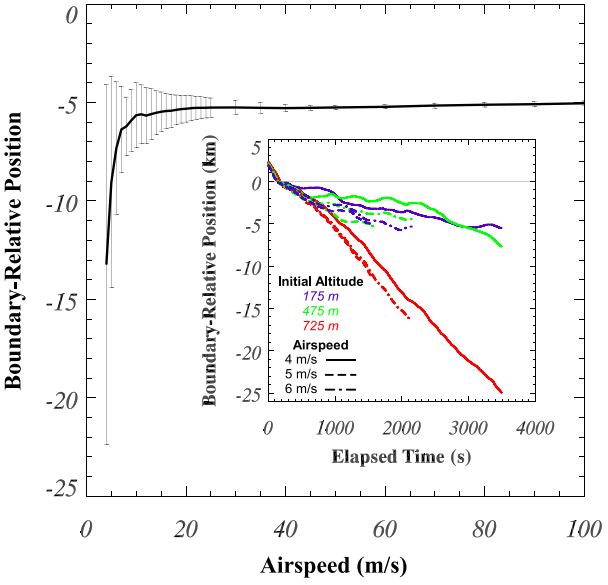

FIG. 3. Mean boundary-relative position of fixed-wing flight termination in the airmass boundary experiments (black curve) along with a spread of one standard deviation (error bars). Mean and standard deviation are calculated using the three flight altitudes and four starting positions for a given airspeed. Inset illustrates boundary-relative flight positions as a function of elapsed time for the three flight altitudes and the three slowest airspeeds considered.

is based on 1-s model output (no temporal interpolation is performed). The synthetic temperature obtained through interpolation from model data without consideration of sensor response will be referred to as the "actual temperature." Synthetic temperature that accounts for sensor response will be referred to as the "observed temperature." The impact of sensor response is modeled assuming a first-order sensor:

$$\frac{d\hat{T}}{dt} = \frac{T_0 - \hat{T}}{\tau}, \tag{1}$$

where $\hat{T}$ is the observed temperature, T_0 is the actual temperature, and τ is the sensor response time. Equation (1) has the solution $\hat{T}(n) = \hat{T}(n-1) + (\Delta t/\tau)[T_0(n) - \hat{T}(n-1)]$, where $n-1$ indicates the previous time increment, and Δt is the time step (equal to 1 s for this work). Observed temperature is linearly interpolated to a 0.1-s time step. Experiments involve sensor responses ranging from 0.1 to 20 s (a total of 48 sensor response times are considered: 0.1, 0.2, 0.3, . . . , 1.0, 1.5, 2.0, . . . , 20 s). Sensor aspiration is assumed to be sufficient across the entire parameter space. Differences between $\hat{T}$ and T_0 along a flight will be referred to as "instantaneous" errors.

3. Results

a. CBL

The well-mixed boundary layer that develops in the simulated CBL yields an expected signal in the observed temperature "collected" by vertical profiling aircraft when the sensor response time increases (Fig. 4a). Namely, the observed temperature is too warm aloft by an amount that scales directly with the sensor response time. When considering the ascent rate as well (Fig. 5), results from flights at location A are consistent with expectations: both maximum absolute instantaneous errors (Fig. 5a) and root-mean-square instantaneous errors (Fig. 5b; calculated over all points

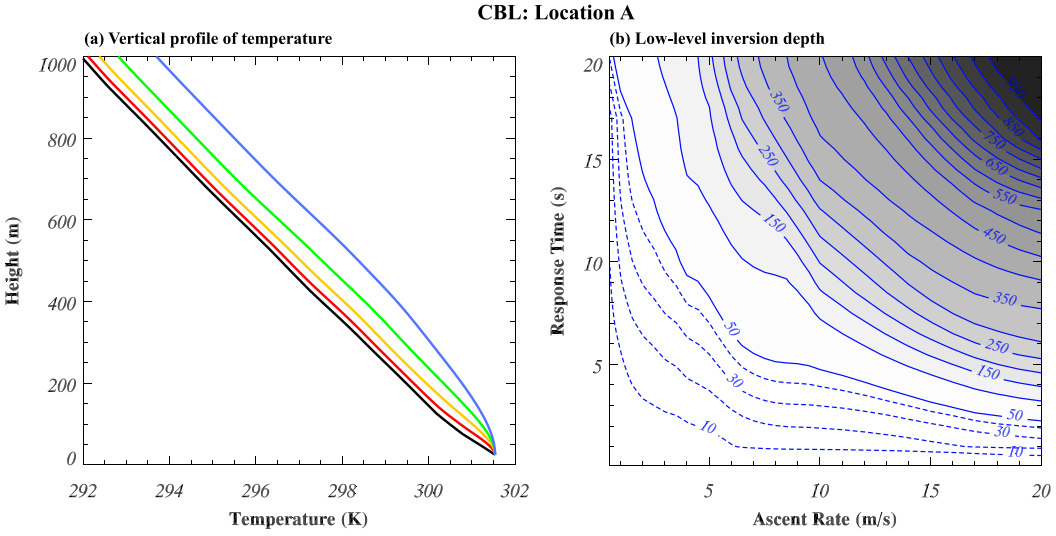

FIG. 4. (a) Vertical profiles of temperature retrieved from rotary-wing flights within the CBL simulation at location A with an ascent rate of 10 m s^{-1}: actual profile (black), profile for $\tau = 2$ s (red), $\tau = 5$ s (orange), $\tau = 10$ s (green), and $\tau = 20$ s (blue). (b) Low-level inversion depths artificially created as a result of observation errors: contoured (continuous curves) and shaded every 50 m; broken contour interval is 10 m (seven-point boxcar smoother applied).

in a given flight) scale directly with the response time and directly with the ascent rate. More specifically, it is apparent that maximum errors are less than typical temperature sensor accuracies (± 0.5 K) as long as ascent rates are less than ~ 10 m s^{-1} and sensor response times are less than ~ 5 s. For sensor response times < 2 s, ascent rates up to ~ 20 m s^{-1} yield maximum errors ≤ 0.5 K.

Observation errors in the low levels also have the effect of smearing out the near-surface superadiabatic layer (Fig. 4) and replacing it with an artificial inversion. This impact is quantified in Fig. 4b through calculation of the depth (from the lowest scalar level at $z = 25$ m) over which the lapse rate $-\partial T/\partial z$ is less than 0.009 K m^{-1} (referred to as low-level inversion depth). While any nonzero low-level inversion depth is erroneous, it is clear from Fig. 4b that the $\sim$125-m-deep superadiabatic layer (Fig. 4) is wholly replaced by an inversion for sensor response times > 10 s and ascent rates > 10 m s^{-1}. For response times < 2 s, ascent rates up to ~ 4 m s^{-1} yield artificial inversion depths of <10 m.

Although flights at location A pass through boundary layer thermals (manifested in the vertical motion apparent in Fig. 6a), it is not immediately obvious whether the temperature perturbations associated with these thermals are important for generating errors resulting from sensor response or airspeed. To evaluate this further, the domain-averaged vertical profile of temperature at $t =$ 2018:03 UTC (the center of the observation periods of all flights) is calculated and rotary-wing aircraft flights are executed through this profile. Differences between the errors associated with these flights and the errors associated with flights through the full temperature field at location A (Figs. 5c,d) are found to be very small (RMSE differences are generally less than 1% of the RMSE for flights through the full temperature field).

As another test of the importance of thermals on instantaneous error generation, errors are calculated for simulated flights from location B (Fig. 1a). A strong boundary layer thermal is present at location B at the center time of all flights (Fig. 1c), thereby guaranteeing that all flights encounter this thermal. The vertical motion encountered during flights from location B is considerably larger than that encountered during flights from location A (Fig. 6). Maximum absolute errors and RMSE are also larger at location B (cf. Figs. 5a,b and Figs. 7a,b). However, the overall pattern of errors as a function of response time and ascent rate is unchanged. Similarly, differences from the domain-averaged vertical profile (Figs. 7c,d) are very small (RMSE differences are generally less than 5% of the RMSE for flights through the full temperature field). Therefore, it is concluded that instantaneous errors resulting from sensor response and ascent rate for rotary-wing aircraft profiles in the CBL simulated for this work are attributable to the background lapse rate and are largely independent of temperature perturbations associated with convective thermals.

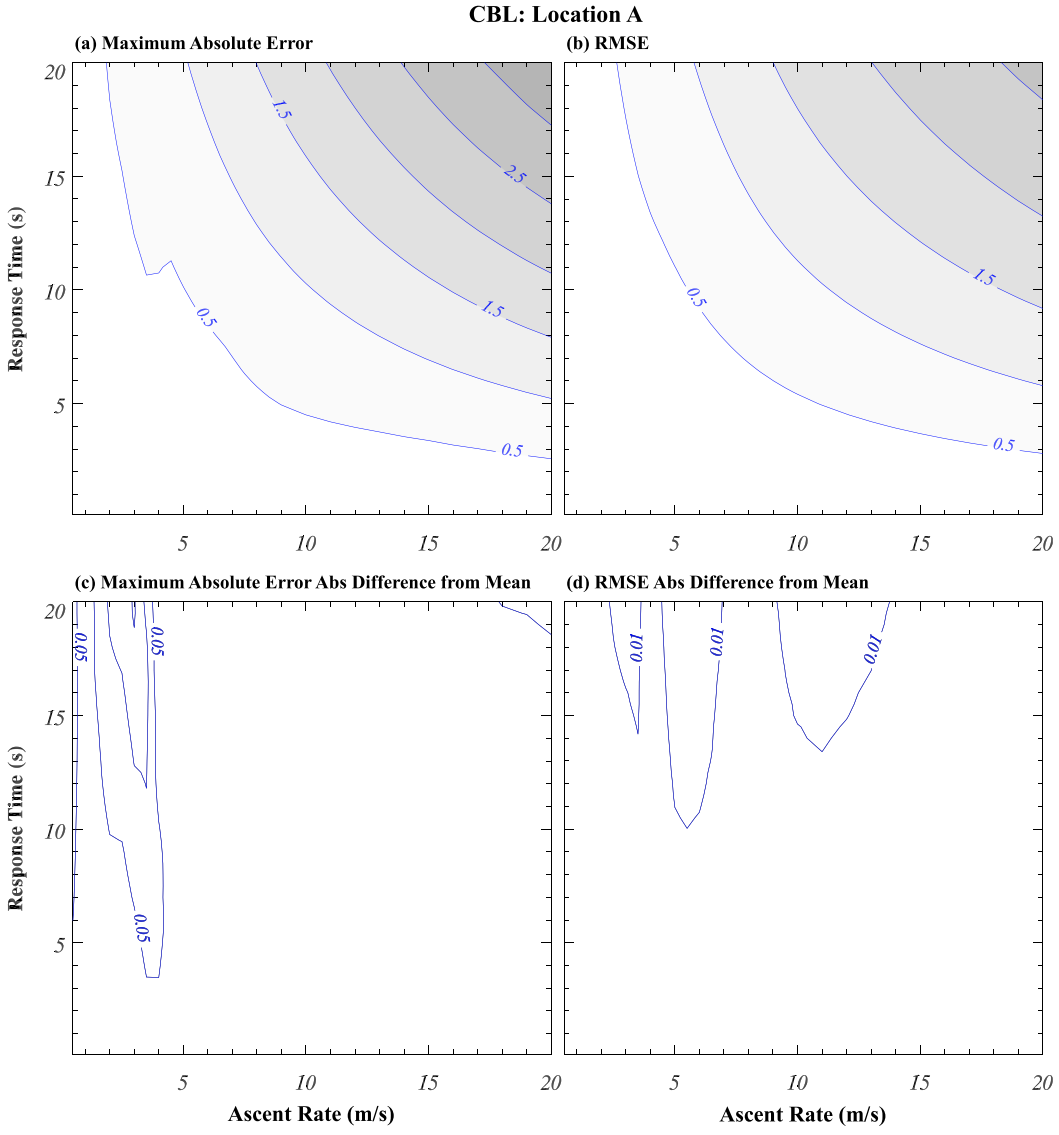

FIG. 5. Errors for rotary-wing aircraft flights in the CBL simulation from position A. Instantaneous errors contoured every 0.5 K: (a) maximum absolute error and (b) RMSE. Absolute differences between the errors calculated using the full temperature field and the errors calculated using the domain-averaged vertical profile of temperature: (c) absolute differences in the maximum absolute error, contoured every 0.05 K, and (d) absolute differences in the RMSE, contoured every 0.01 K.

b. *Airmass boundary*

As with the flights through the CBL simulation, flights across the simulated airmass boundary illustrate the expected sensitivity to sensor response time (Fig. 8). Errors as a function of both sensor response time and airspeed appear in Fig. 9. For a given combination of airspeed and sensor response time, errors are calculated across all four transects initialized a distance δx_b ahead of the airmass boundary (refer to section 2b). Errors generally increase with increasing airspeed and increasing sensor response time (Fig. 9). For all flight altitudes, maximum absolute errors (Figs. 9a–c) are $\leq$0.5 K for airspeeds less than $\sim$10 m s^{-1} and sensor response times less than $\sim$1.5 s. Compared to flights through the simulated CBL (Figs. 5a, 7a), this is a more restrictive set of conditions on the flight characteristics required to yield accurate observations. In contrast, the RMSE for the airmass boundary flights (Figs. 9d–f) is considerably less than the RMSE for CBL flights (Figs. 5b, 7b). CBL flights experience instantaneous errors over nearly the entire

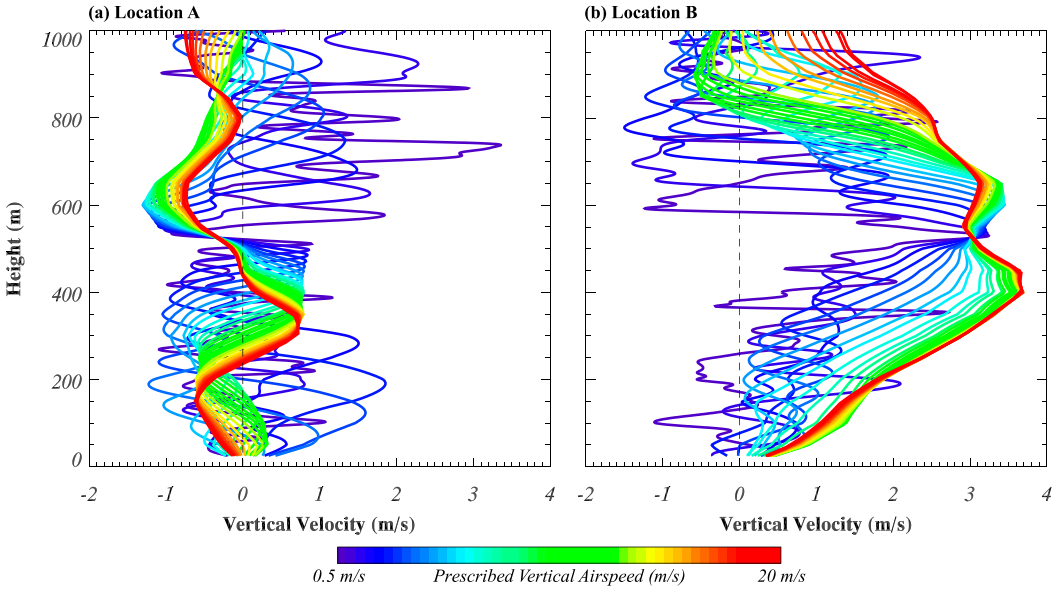

FIG. 6. Actual vertical velocity at the position of the aircraft during profiles of rotary-wing aircraft in the simulated CBL. (a) Location A and (b) location B.

flight (Fig. 4) as a consequence of the nearly constant $\partial T/\partial z \sim -10\,\mathrm{K\,km^{-1}}$ through which they operate. However, since the air masses on either side of the airmass boundary have spans where $|\partial T/\partial x|$ is small ($\ll 10\,\mathrm{K\,km^{-1}}$) and/or oscillatory (Fig. 8), airmass boundary flights have spans in which instantaneous errors do not accumulate like they would if $|\partial T/\partial x|$ were constant and/or large.

As discussed in section 1, the accuracy with which serial observations represent a snapshot of the atmosphere likely scales inversely with airspeed. In an effort to quantify the degree to which this relationship holds in light of the opposite dependence of instantaneous errors on airspeed, differences in observed temperature along a flight are calculated relative to representative snapshots.

Representative snapshots are defined as the state of the atmosphere at a particular time within the observation period of a particular transect that best matches the actual (time dependent) values along the transect. A representative snapshot of temperature $T_0(x)$ exhibits the best "fit," in a least squares sense, to the time series of actual (not observed) temperature $T_0(t)$ at each point along a particular transect. Fitting is achieved through time-to-space conversion into a boundary-relative frame of reference (boundary position is updated for each analysis time). If the boundary-relative structure of the density current did not change in time, then the state of the density current at every time along the transect could be the representative snapshot. The boundary-relative position of the aircraft corresponding to the time of a representative snapshot can also be interpreted as the position at which the time scale of density current variability is the shortest and, thus, where the time difference between the state of the atmosphere and the observations collected by the aircraft must be minimized. Symbolically, the snapshot is the state at a particular time t_n that minimizes $\left\{\sum_i^N (1/N)[T_0(t_n, x_i) - T_0(t_i, x_i)]^2\right\}^{1/2}$, where N is the number of points along a transect; T_0 is the actual (not observed) temperature; and (t_i, x_i) are the time and boundary-relative position of the aircraft along the transect, respectively.

For the simulations conducted, the boundary-relative positions of the aircraft at the time of a representative snapshot typically do not correspond to the location of the airmass boundary (Fig. 10) but are instead "behind" the boundary near or within the density current wake (Fig. 2). This is particularly true of flights at an altitude of 475 and 725 m, since the turbulent wake penetrates below these levels (Fig. 2). Thus, it is behind the boundary where the time scale of density current variability is the shortest and, thus, where the time difference between the state of the atmosphere and the observations collected by the aircraft must be minimized. In these locations, the time evolution of the density current means that the state of the atmosphere will rapidly diverge from the state represented at the snapshot time.

Disregarding the instantaneous errors resulting from sensor response, the RMSE of actual temperature

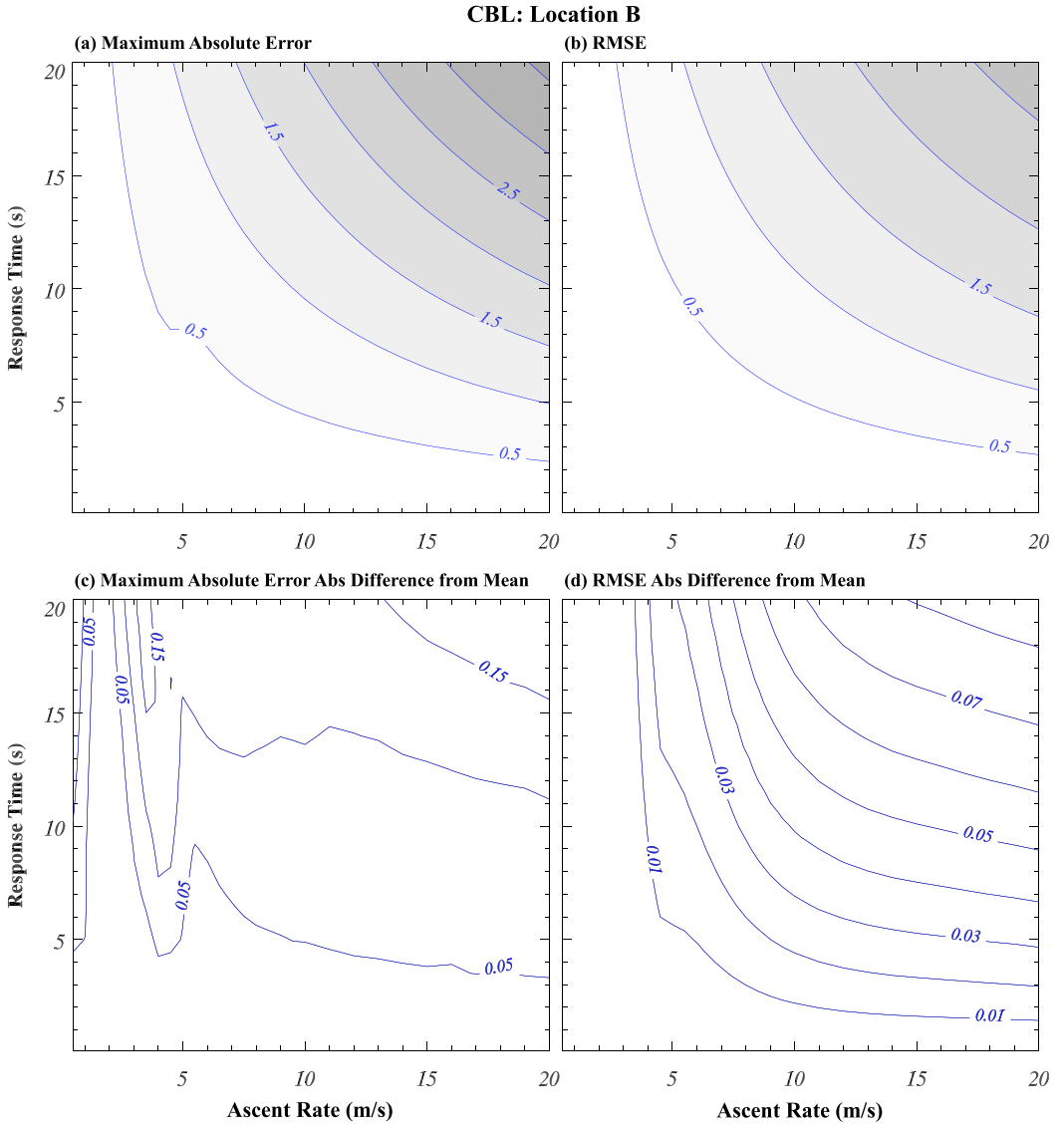

FIG. 7. As in Fig. 5, but for flights at location B.

values along transects (calculated over all transect points and all four values of δx_b) relative to the temperature of the representative snapshot generally increases with decreasing airspeed (black curves in Fig. 11). The trend is more pronounced, and maximum errors are larger for flights that encounter the density current wake (e.g., flight altitudes of 475 and 725 m; Figs. 11a,b). When considering representation errors that also include instantaneous errors resulting from sensor response (i.e., representation errors calculated using the observed temperature instead of actual temperature), instantaneous errors for the $z = 175$-m flights are dominant compared to representation errors for nearly all sensor response times (Fig. 11c). However, for flights that encounter the wake, sensor response times generally need to exceed ~5 s before instantaneous errors become larger than errors in representation (Figs. 11a,b).

4. Discussion

Based on these results, an approximation for the errors resulting from sensor response and flight speed for previous applications of sUAS can be made. During the Collaborative Colorado–Nebraska UAS Experiment (CoCoNUE; Houston et al. 2012), the NexSTAR fixed-wing sUAS was flown across a cold front and an outflow boundary using a pressure, temperature, and humidity sonde originally developed for use in the Miniature In Situ Sounding

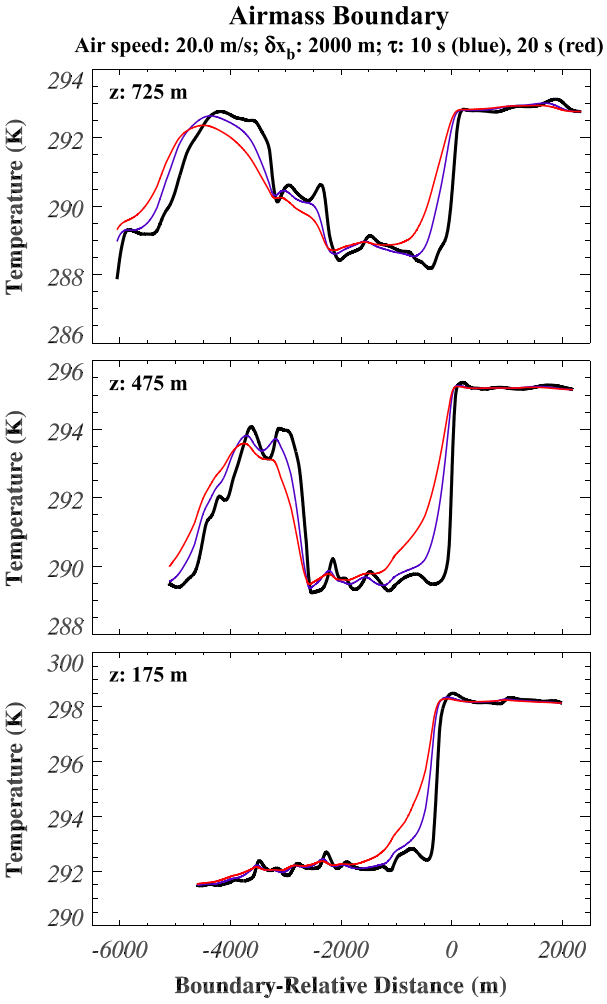

FIG. 8. Boundary-relative profiles of temperature retrieved from the airmass boundary simulation. The visualization of transect data in a boundary-relative frame of reference is similar to that of Riganti and Houston (2017) and Hanft and Houston (2018). Negative distance indicates the cold side of the boundary. Actual profiles (black), profiles for $\tau = 10$ s (blue), and profiles for $\tau = 20$ s (red).

Technology (MIST) dropsonde designed by the In-Situ Sensing Facility at NCAR's Earth Observing Laboratory (this sonde is based on the Vaisala RS92 core[1]). Air speeds were nominally 20 m s^{-1} and the manufacturer-specified sensor response was 0.4 s. Both transects were below the wake, and thus based on the results from the present work, maximum absolute errors were ~±0.3 K and the RMSE was ~0.025 K. During the Second Verification of the Origins of Rotation in Tornadoes Experiment (VORTEX2), a Tempest fixed-wing sUAS was operated across the rear-flank gust front of the "Last Chance, Colorado" supercell on 10 June 2010 (Riganti and Houston 2017). Like the NexSTAR, the nominal airspeed was 20 m s^{-1} and the MIST sonde was used. Since this flight crossed into the outflow wake (Riganti and Houston 2017), the present results would indicate that absolute errors were ~±0.3 K and the RMSE was ~0.03 K.

As an example of CBL flights, the multirotor profiles of Hemingway et al. (2017) will be used. These flights used a 3D Robotics (3DR) Iris+ outfitted with an International Met Systems (iMet) XQ pressure, temperature, and humidity sensor. Ascent rates were ~2 m s^{-1}. The manufacturer-specified sensor response time of the iMet-XQ is 2 s, but this is based on stagnant conditions (M. Benoit 2018, personal communication). Based on subsequent testing, the response time is likely to be <1 s (M. Benoit 2018, personal communication). Assuming sensor response times of 1 s (2 s), the maximum absolute errors were ~±0.04 K (~±0.08 K) and the RMSE was ~0.02 K (~0.05 K).

In section 3b it is noted that the RMSE is smaller for the airmass boundary experiments than for the CBL experiments because, unlike a CBL where an along-flight temperature gradient of approximately −10 K km^{-1} is to be expected, airmass boundaries have spans on either side of the boundary where the along-flight temperature gradient is small. Thus, if the RMSE were used in isolation, the impact of the boundary (or the wake where gradients are also large) would be diluted. If data collection is to be directed toward the boundary or the wake, the maximum absolute error and not RMSE should be used to guide decisions on the configuration and operation of airborne systems.

While airmass boundaries and the CBL are common focuses for research in the atmospheric boundary layer, characteristics of their structure that are germane to error generation from sensor response and flight speed will vary from case to case. For example, the strength of thermals within a CBL will depend on time of day, time of year, latitude, surface characteristics (e.g., albedo), cloud cover, and vertical profile of wind, among others. The experiments conducted for this work utilize values for these conditions (section 2a) that are away from extreme values that could be used. Nevertheless, only a single CBL LES is considered. However, given the minimal importance of thermals on the simulated errors, the authors posit that the results presented for the sensitivity of errors to sensor response and rotary-wing ascent rate in the CBL are fairly generalizable.

[1] For more information on the RS92 sonde, the reader is referred to https://www.vaisala.com/sites/default/files/documents/RS92SGP-Datasheet-B210358EN-F-LOW.pdf. For more information on the MIST sonde, the reader is referred to Cohn et al. (2013).

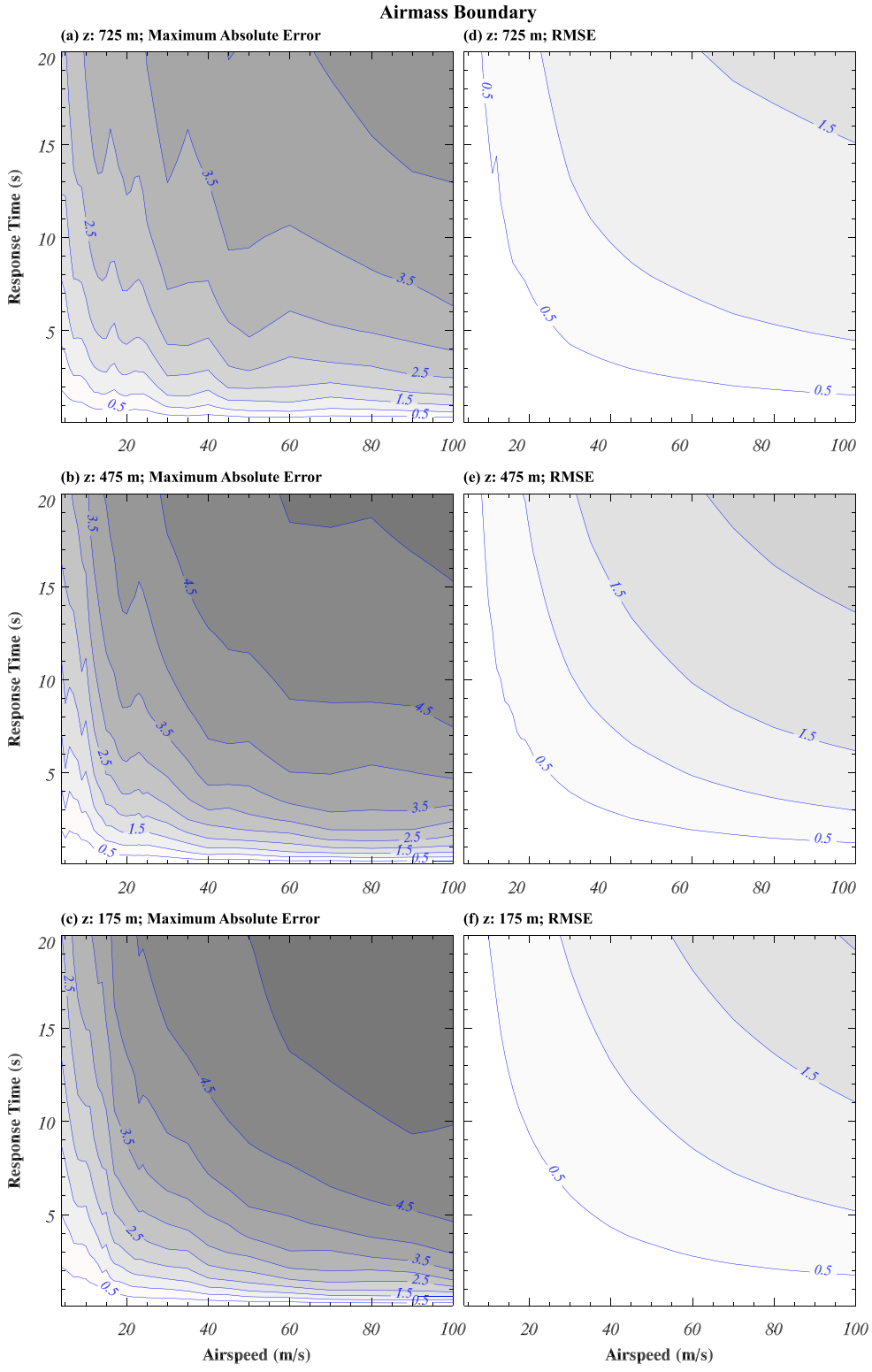

FIG. 9. As in Fig. 5, but for the airmass boundary flights at altitudes of (a),(d) 725, (b),(e) 475, and (c),(f) 175 m.

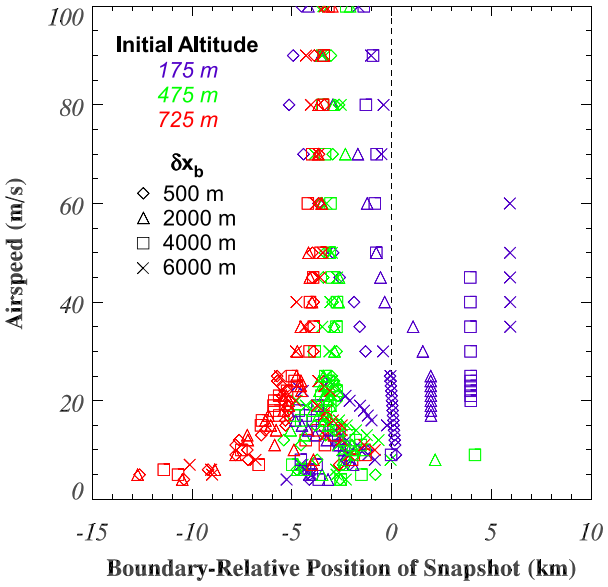

FIG. 10. Boundary-relative location of the aircraft for the representative snapshot for all of the airmass-boundary flights. Flights at an altitude of 175 m (purple), 475 m (green), and 725 m (red), and flights launched at δx_b values of 500 m (diamonds), 2000 m (triangles), 4000 m (squares), and 6000 m (crosses).

The characteristic of airmass boundaries most likely to impact errors from sensor response and flight speed is the temperature deficit in the dense air. It can be shown theoretically that, for a given aircraft airspeed, both maximum absolute errors and the RMSE resulting from sensor response scale directly with the magnitude of the temperature deficit. As in the CBL simulation, in the airmass boundary simulation, the temperature deficit generated using the free parameters described in section 2a is away from the extreme values that have been observed (a ~6-K deficit is encountered by the simulated aircraft). However, since only a single airmass boundary is considered, the application of these results to guide decisions on the configuration and operation of small unmanned aircraft systems tasked to sample airmass boundaries must be placed in the context of the temperature deficit used for this work.

5. Summary

The impact of sensor response and aircraft airspeed on the accuracy of in situ temperature observations of the CBL and airmass boundaries were estimated using simulated aircraft flown within LES. Aircraft models for both rotary-wing and fixed-wing platforms were designed to be simple and physically reasonable with synthetic data retrieved assuming a well-aspirated first-order sensor. Rotary-wing aircraft are operated as profilers in the simulated CBL, and fixed-wing aircraft are operated through transects across the simulated airmass boundary.

Instantaneous errors are found to scale directly with sensor response time and airspeed for all experiments. Maximum errors for rotary-wing flights in the simulated CBL are less than 0.5 K as long as ascent rates are less than $\sim 10\,\mathrm{m\,s^{-1}}$, and sensor response times are less than ~5 s. For sensor response times < 2 s, ascent rates up to $\sim 20\,\mathrm{m\,s^{-1}}$ yield errors ≤ 0.5 K. Errors also manifest in a smearing out of the near-surface superadiabatic layer and the creation of an artificial inversion. For response times < 2 s, ascent rates up to $\sim 4\,\mathrm{m\,s^{-1}}$ yield artificial inversion depths of <10 m. For fixed-wing flights across airmass boundaries, maximum absolute errors are ≤ 0.5 K for airspeeds less than $\sim 10\,\mathrm{m\,s^{-1}}$ and sensor response times less than ~1.5 s—a more restrictive set of conditions on the flight characteristics are required to yield accurate observations compared to the CBL. When rotary-wing profiles are executed in the domain-averaged vertical profile of temperature (which excludes turbulent temperature perturbations), instantaneous errors were found to be very similar to errors from the full temperature field. Thus, instantaneous errors for rotary-wing aircraft profiles in the CBL simulated for this work were principally attributable to the background lapse rate.

For airmass boundary flights, errors in representation (relative to a representative snapshot) were also evaluated. For the simulations conducted, representative snapshots across all flights do not typically correspond to the location of the aircraft as it passes near the airmass boundary but instead correspond to locations "behind" the boundary near or within the density current wake. This is a direct consequence of the fact that, for the density current simulated for this work, in a boundary-relative frame of reference, the boundary evolves much slower than the turbulent wake trailing the density current head. In general, the representation accuracy is found to degrade with decreasing airspeed. This signal is most pronounced for flights that encounter the density current wake. When representation errors are also included along with instantaneous errors resulting from sensor response, instantaneous errors were found to be dominant for flights that remain below the turbulent wake. However, for flights that encounter the wake, sensor response times generally need to exceed ~5 s before instantaneous errors become larger than errors in representation.

Acknowledgments. This work has been supported by National Science Foundation Grants OIA-1539070 and IIS-1527113.

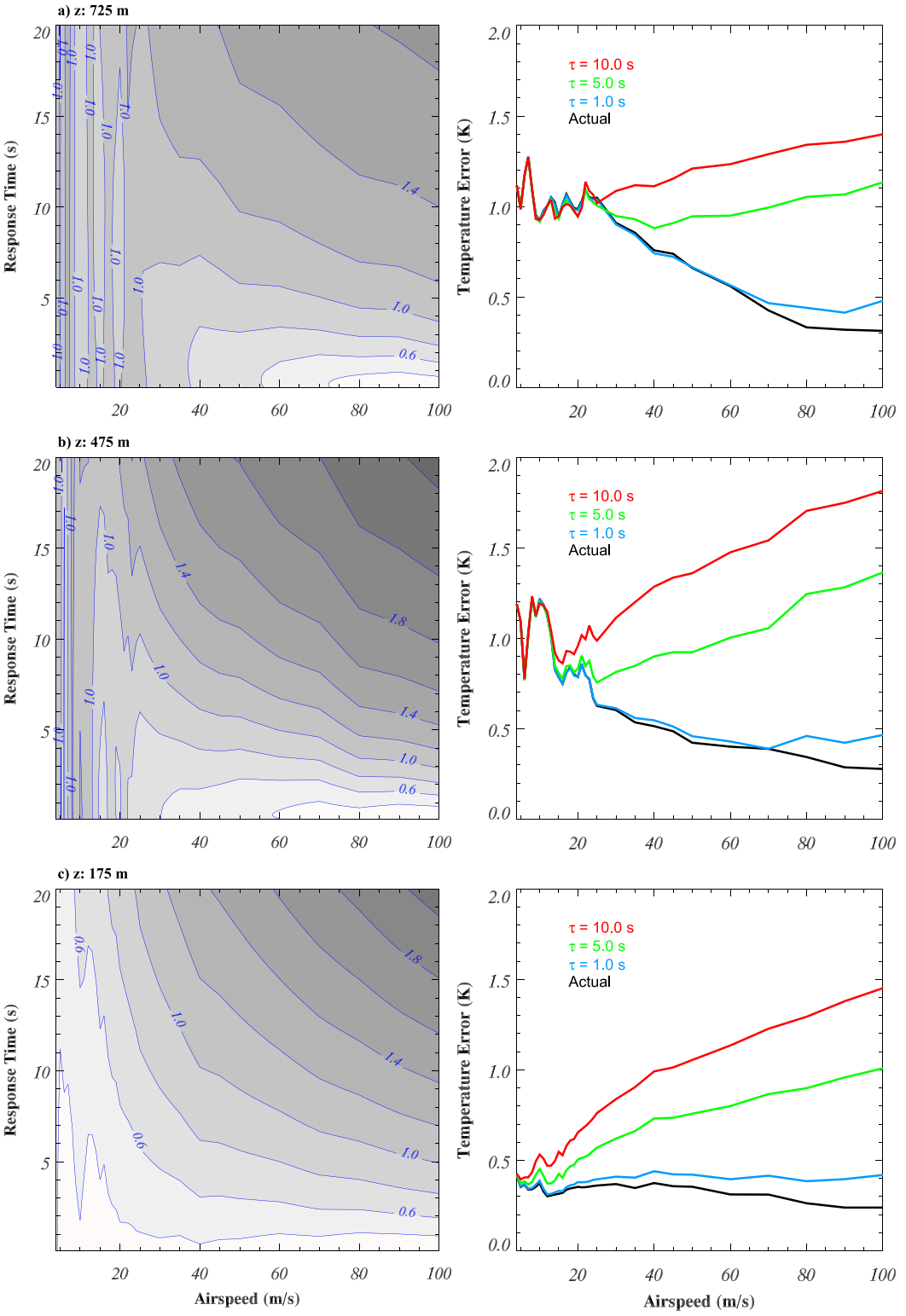

FIG. 11. RMSE relative to representative snapshots for each flight for (a) $z = 725$ m, (b) $z = 475$ m, and (c) $z = 175$ m. (left) Errors contoured every 0.2 K relative to airspeed and response time. (right) Errors plotted as a function of airspeed for response times of 1, 5, and 10 s along with the errors for the actual data.

REFERENCES

Bryan, G. H., and J. M. Fritch, 2002: A benchmark simulation for moist nonhydrostatic numerical models. *Mon. Wea. Rev.*, **130**, 2917–2928, https://doi.org/10.1175/1520-0493(2002)130<2917:ABSFMN>2.0.CO;2.

Burns, S. P., and Coauthors, 1999: Comparisons of aircraft, ship, and buoy meteorological measurements from TOGA COARE. *J. Geophys. Res.*, **104**, 30 853–30 883, https://doi.org/10.1029/1999JD900934.

Carlson, T. N., and F. E. Boland, 1978: Analysis of urban-rural canopy using a surface heat flux/temperature model. *J. Appl. Meteor.*, **17**, 998–1013, https://doi.org/10.1175/1520-0450(1978)017<0998:AOURCU>2.0.CO;2.

Chen, C., 1995: Numerical simulations of gravity currents in uniform shear flows. *Mon. Wea. Rev.*, **123**, 3240–3253, https://doi.org/10.1175/1520-0493(1995)123<3240:NSOGCI>2.0.CO;2.

Cohn, S. A., and Coauthors, 2013: Driftsondes: Providing in situ long-duration dropsonde observations over remote regions. *Bull. Amer. Meteor. Soc.*, **94**, 1661–1674, https://doi.org/10.1175/BAMS-D-12-00075.1.

Droegemeier, K. K., and R. B. Wilhelmson, 1987: Numerical simulation of thunderstorm outflow dynamics. Part I: Outflow sensitivity experiments and turbulence dynamics. *J. Atmos. Sci.*, **44**, 1180–1210, https://doi.org/10.1175/1520-0469(1987)044<1180:NSOTOD>2.0.CO;2.

Dudhia, J., 1996: A multi-layer soil temperature model for MM5. Preprints, *Sixth PSU/NCAR Mesoscale Model Users' Workshop*, Boulder, CO, PSU and NCAR, 49–50.

——, D. Gill, K. Manning, W. Wang, and C. Bruyere, 2004: PSU/NCAR mesoscale modeling system tutorial class notes and user's guide (MM5 modelling system version 3). UCAR, 390 pp.

Elston, J. S., J. Roadman, M. Stachura, B. Argrow, A. L. Houston, and E. W. Frew, 2011: The Tempest Unmanned Aircraft System for in situ observations of tornadic supercells: Design and VORTEX2 flight results. *J. Field Rob.*, **28**, 461–483, https://doi.org/10.1002/rob.20394.

——, B. Argrow, M. Stachura, D. Weibel, D. Lawrence, and D. Pope, 2015: Overview of small fixed-wing unmanned aircraft for meteorological sampling. *J. Atmos. Oceanic Technol.*, **32**, 97–115, https://doi.org/10.1175/JTECH-D-13-00236.1.

Frew, E. W., J. Elston, B. Argrow, A. L. Houston, and E. N. Rasmussen, 2012: Unmanned aircraft systems for sampling severe local storms and related phenomena. *IEEE Rob. Autom. Mag.*, **19**, 85–95, https://doi.org/10.1109/MRA.2012.2184193.

Hanft, W., and A. L. Houston, 2018: An observational and modeling study of mesoscale air masses with high theta-e. *Mon. Wea. Rev.*, **146**, 2503–2524, https://doi.org/10.1175/MWR-D-17-0389.1.

Hemingway, B., A. Frazier, B. Elbing, and J. Jacob, 2017: Vertical sampling scales for atmospheric boundary layer measurements from small unmanned aircraft systems (sUAS). *Atmosphere*, **8**, 176, https://doi.org/10.3390/atmos8090176.

Houston, A. L., 2016: The sensitivity of deep ascent of cold-pool air to vertical shear and cold-pool buoyancy. *Electron. J. Severe Storms Meteor.*, **11** (3), http://www.ejssm.org/ojs/index.php/ejssm/article/viewArticle/151.

——, B. Argrow, J. Elston, J. Lahowetz, E. W. Frew, and P. C. Kennedy, 2012: The Collaborative Colorado–Nebraska Unmanned Aircraft System Experiment. *Bull. Amer. Meteor. Soc.*, **93**, 39–54, https://doi.org/10.1175/2011BAMS3073.1.

Kiefer, C. M., C. B. Clements, and B. E. Potter, 2012: Application of a mini unmanned aircraft system for in situ monitoring of fire plume thermodynamic properties. *J. Atmos. Oceanic Technol.*, **29**, 309–315, https://doi.org/10.1175/JTECH-D-11-00112.1.

Knuth, S. L., and J. J. Cassano, 2014: Estimating sensible and latent heat fluxes using the integral method from in situ aircraft measurements. *J. Atmos. Oceanic Technol.*, **31**, 1964–1981, https://doi.org/10.1175/JTECH-D-14-00008.1.

Lee, B. D., and R. B. Wilhelmson, 1997: The numerical simulation of nonsupercell tornadogenesis. Part I: Initiation and evolution of pretornadic misocyclone circulations along a dry outflow boundary. *J. Atmos. Sci.*, **54**, 32–60, https://doi.org/10.1175/1520-0469(1997)054<0032:TNSONS>2.0.CO;2.

Liu, C., and M. W. Moncrieff, 1996: A numerical study of the effects of ambient flow and shear on density currents. *Mon. Wea. Rev.*, **124**, 2282–2303, https://doi.org/10.1175/1520-0493(1996)124<2282:ANSOTE>2.0.CO;2.

Lundquist, J. K., M. J. Churchfield, S. Lee, and A. Clifton, 2015: Quantifying error of lidar and sodar Doppler beam swinging measurements of wind turbine wakes using computational fluid dynamics. *Atmos. Meas. Tech.*, **8**, 907–920, https://doi.org/10.5194/amt-8-907-2015.

Maronga, B., A. F. Moene, D. van Dinther, S. Raasch, F. C. Bosveld, and B. Gioli, 2013: Derivation of structure parameters of temperature and humidity in the convective boundary layer from large-eddy simulations and implications for the interpretation of scintillometer observations. *Bound.-Layer Meteor.*, **148**, 1–30, https://doi.org/10.1007/s10546-013-9801-6.

McCarthy, J., 1973: A method for correcting airborne temperature data for sensor response time. *J. Appl. Meteor.*, **12**, 211–214, https://doi.org/10.1175/1520-0450(1973)012<0211:AMFCAT>2.0.CO;2.

Monin, A. S., and A. M. Obukhov, 1954: Basic laws of turbulent mixing in the atmosphere near the ground. *Tr. Geofiz. Inst., Akad. Nauk SSSR*, **24**, 163–187.

Nowotarski, C. J., P. M. Markowski, Y. P. Richardson, and G. H. Bryan, 2014: Properties of a simulated convective boundary layer in an idealized supercell thunderstorm environment. *Mon. Wea. Rev.*, **142**, 3955–3976, https://doi.org/10.1175/MWR-D-13-00349.1.

Reineman, B. D., L. Lenain, N. M. Statom, and W. K. Melville, 2013: Development and testing of instrumentation for UAV-based flux measurements within terrestrial and marine atmospheric boundary layers. *J. Atmos. Oceanic Technol.*, **30**, 1295–1319, https://doi.org/10.1175/JTECH-D-12-00176.1.

Riganti, C. J., and A. L. Houston, 2017: Rear-flank outflow dynamics and thermodynamics in the 10 June 2010 Last Chance, Colorado, supercell. *Mon. Wea. Rev.*, **145**, 2487–2504, https://doi.org/10.1175/MWR-D-16-0128.1.

Scipion, D., R. D. Palmer, P. B. Chilson, E. Fedorovich, and A. Botnick, 2009: Retrieval of convective boundary layer wind field statistics from radar profiler measurements in conjunction with large eddy simulation. *Meteor. Z.*, **18**, 175–187, https://doi.org/10.1127/0941-2948/2009/0371.

Skamarock, W. C., and Coauthors, 2008: A description of the Advanced Research WRF version 3. NCAR Tech. Note NCAR/TN-475+STR, 113 pp., http://dx.doi.org/10.5065/D68S4MVH.

van den Kroonenberg, A. C., S. Martin, F. Beyrich, and J. Bange, 2012: Spatially-averaged temperature structure parameter over a heterogeneous surface measured by an unmanned aerial vehicle. *Bound.-Layer Meteor.*, **142**, 55–77, https://doi.org/10.1007/s10546-011-9662-9.

Wainwright, C. E., T. A. Bonin, P. B. Chilson, J. A. Gibbs, E. Fedorovich, and R. D. Palmer, 2015: Methods for evaluating the temperature structure-function parameter using unmanned aerial systems and large-eddy simulation. *Bound.-Layer Meteor.*, **155**, 189–208, https://doi.org/10.1007/s10546-014-0001-9.